On quantum transport in flat-band materials

Oriekhov, D.

Chapter 6

Orbital susceptibility of T-graphene: Interplay of high-order van Hove singularities and Dirac cones

6.1 Introduction

Possible existence of two new graphene allotropes, planar tetragraphene (or octagraphene) and buckled T-graphene composed of carbon octagons with tetrarings, was demonstrated some time ago using the Density Functional Theory (DFT) [52]. Several previous attempts to find such allotropes were made in Refs.[201, 202]. It was noted that planar T-graphene allotrope should be the most stable one after graphene while the buckled T-graphene is not stable, and its fully relaxed state is very similar to planar T-graphene [179]. Recently, the tetragraphene allotrope has been predicted to possess superconductivity with critical temperature up to around 20.8 K [203].

Some geometrical and electronic properties, as well as low-energy physics of octagraphene were studied in Ref.[204], the phase diagrams were analyzed and the existence of Mott metal-insulator phase transitions in the Hubbard model on square-octagon lattice was pointed out in [205–209]. In addition, structural and electronic properties of T-graphene and its modifications were studied by DFT calculations in Refs.[210–213] and the kinetic stability with time was analyzed in Ref.[214]. Later, it was shown

[53] that the 2D monolayers of Zn_2O_2 and Zn_4O_4 also have nearly ideal square-octagon lattice. In recent paper [53] the stability of multilayer materials such as ZnO composed of square-octagon lattice was studied with the help of DFT technique. Also it was shown that MoS_2 transition metal dichalcogenide with square-octagon lattice can possess Dirac fermions with Fermi velocity comparable to that of graphene [207]. The coexistence of Dirac fermions and nearly flat bands seems to be a very interesting property of square-octagon lattice and motivates us to study physical quantities such as orbital susceptibility in terms on newly introduced concept of high-order van Hove singularities [25].

As is known, when the doping level approaches VHS, system can exhibit strong responses such as orbital paramagnetism in two-dimensional case [50] or chiral superconductivity in the case of graphene [26]. An *ordinary* VHS in two-dimensional electron system corresponds to logarithmic divergence of the density of states (DOS). The distinctive feature of high-order VHS is a more singular, power-law divergence of DOS with an asymmetric peak [25, 215]. At the same time, the recent studies of two-dimensional lattices uncovered a wide family of exotic band structures [15] with flat bands and multi-band touching points, at which the quasiparticles are effectively described by high-pseudospin Hamiltonians. Flat bands can be considered as a limiting case of VHS with delta-function divergence of DOS.

The prominent examples of materials with high-order VHS of different kind are bilayer graphene with tuned dispersion with the help of an interlayer voltage bias [216], $Sr_3Ru_2O_7$ [217] and $\beta - YbAlB_4$ [218]. Recently it was also shown that when a high-order VHS is placed close to the Fermi level, density wave, Pomeranchuk orders, and superconductivity can all be enhanced [27]. The role of high-order VHS on different types of instabilities in twisted bilayer graphene was analyzed in Ref.[219]. The presence of van Hove singularities in twisted bilayer graphene [220] can lead to valley magnetism [221], density waves and unconventional superconductivity [222] such as topological and nematic superconductivity [223], the so-called "high-T_c" phase diagram [28], Kohn-Luttinger superconductivity [224].

The orbital susceptibility [225] measures the response of a time-reversal invariant electronic system to an external magnetic field. To evaluate susceptibility of T-graphene analytically and numerically we use the formulas for susceptibility derived in Refs.[226] and [227]. We analyze the

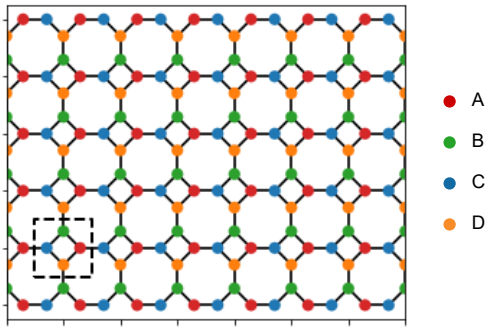

Figure 6.1. T-graphene lattice structure, which is described in main text. Each sublattice is denoted by its own color. Black dashed rectangle encircles one elementary cell. The hopping parameters between two small squares are t_1 and inside each small square - t_2.

role of VHS of both kinds in orbital susceptibility for electrons on square-octagon lattice. Particularly, we show that the flat lines in tight-binding band structure, which were firstly mentioned in Ref.[206], also represent high-order VHS with inverse square root divergence of DOS.

The paper is organized as follows. In Sec.6.2 we describe the tight-binding Hamiltonian of square-octagon lattice. Then, in Sec.6.3 we derive effective low-energy Hamiltonians that describe bands around highly-symmetric points in Brillouin zone (BZ). Also we identify the type of VHS which are present in T-graphene. In Sec.6.4 we perform numerical evaluation of susceptibility, and then analyze the qualitative physical effects of Dirac cones (Sec.6.4.2) and VHS using effective low-energy expansion (Secs. 6.4.3 and 6.4.4). The role of high-order VHS is discussed also in the Conclusions (Sec.6.5) where we summarize the obtained results. In Appendix 6.6 we analyze flat lines in the dispersion of middle bands, and in Appendix 6.7 we present expressions for the Green's functions of tight-binding and Löwdin Hamiltonians.

6.2 Tight-binding model

The square-octagon lattice consists of four atoms per unit cell which form a small square, and is shown on Fig.6.1. According to Ref.[202], the numerical values for all nearest neighbor interatomic distances are approximately equal to 1.429Å and lattice constant $a = 3.47$Å for T-graphene. Ref.[204]

gives the intra-square, 1.48Å, and inter-squares, 1.35Å, distances, and similar values were reported in Ref.[53]. The basis vectors of Bravais lattice and reciprocal lattice are

$$\begin{aligned} &\boldsymbol{a}_1 = (a,\ 0), \quad \boldsymbol{a}_2 = (0,\ a); \\ &\boldsymbol{b}_1 = \left(0,\ \frac{2\pi}{a}\right), \quad \boldsymbol{b}_2 = \left(\frac{2\pi}{a},\ 0\right). \end{aligned} \tag{6.1}$$

In the tight-binding model, we take hopping parameters between atoms in two neighboring small squares to be t_1, and inside small square t_2. The corresponding tight-binding Hamiltonian has the form [204, 206]

$$H_{Tg}(\boldsymbol{k}) = -\begin{pmatrix} 0 & t_2 & t_1 e^{ik_x a} & t_2 \\ t_2 & 0 & t_2 & t_1 e^{ik_y a} \\ t_1 e^{-ik_x a} & t_2 & 0 & t_2 \\ t_2 & t_1 e^{-ik_y a} & t_2 & 0 \end{pmatrix}. \tag{6.2}$$

and acts on the four-component wave functions $\psi = (\psi_A, \psi_B, \psi_C, \psi_D)$ (see Fig.6.1 for sublattice labels). The above mentioned difference in interatomic distances can effectively described by tuning the hopping parameters t_1 and t_2. The values of these hopping parameters can be taken from DFT calculations: $t_1 = 2.9\,\text{eV}$ and $t_2 = 2.5\,\text{eV}$ were used in Ref.[204], while $t_1 = 2.98\,\text{eV}$ and $t_2 = 2.68\,\text{eV}$ were found from DFT calculations inside one layer of octagraphene [228].

The spectrum can be found from the equation $\det[\varepsilon\mathbb{I} - H_{Tg}(\boldsymbol{k})] = 0$, which after simplification reduces to [204, 206]

$$\begin{aligned} &\varepsilon^4 - 2\left(t_1^2 + 2t_2^2\right)\varepsilon^2 + 4t_1 t_2^2 \varepsilon\left(\cos\left(ak_x\right) + \cos\left(ak_y\right)\right) - \\ &- 4t_1^2 t_2^2 \cos\left(ak_x\right)\cos\left(ak_y\right) + t_1^4 = 0, \end{aligned} \tag{6.3}$$

and has the form of depressed quartic equation. The spectrum is symmetric with respect to rotations on the angle $\frac{\pi}{4}$ in k-space, because the lattice has a C_4 point symmetry group. Also the spectrum is symmetric with respect to transformations $\varepsilon \to -\varepsilon$ together with $k_x \to k_x \pm \frac{\pi}{a}$, $k_y \to k_y \pm \frac{\pi}{a}$ (called chiral symmetry in [206]). The Brillouin zone of square-octagon lattice is a square with $-\frac{\pi}{a} < k_x, k_y < \frac{\pi}{a}$. The corresponding highly-symmetric points are defined as

$$\begin{aligned} &\Gamma = (0,0), \quad M = \left(\pm\frac{\pi}{a}, \pm\frac{\pi}{a}\right), \\ &X = \left(\pm\frac{\pi}{a}, 0\right),\ \left(0, \pm\frac{\pi}{a}\right), \end{aligned} \tag{6.4}$$

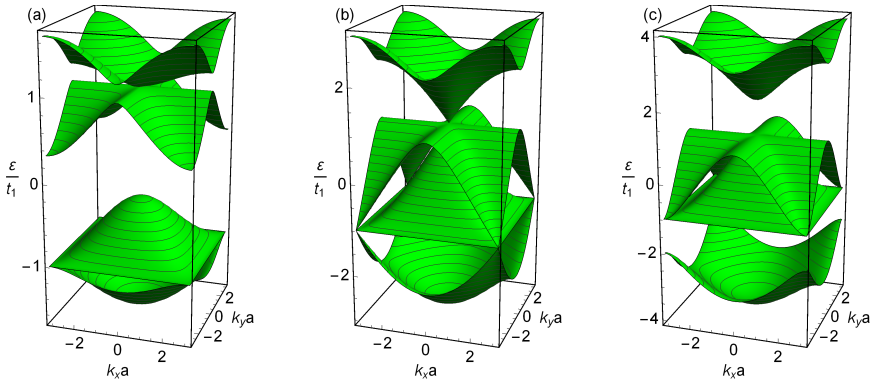

Figure 6.2. Spectrum which is given by Eq.(6.3) for three values of parameter $\alpha = t_2/t_1$: panel (a) $\alpha = \frac{1}{3}$, panel (b) $\alpha = 1$ and panel (c) $\alpha = \frac{3}{2}$. The energy ε is measured in units of hopping parameter t_1. On the panel (b) one can observe the three-band-touching points where the two Dirac cones meet nearly flat middle band. Black lines denote the lines of constant energies.

and are located in the center, corners and the middle of each square site, respectively. It is convenient to measure the energy in terms of t_1 hopping parameter, and introduce the dimensionless ratio of hopping parameters $\alpha = t_2/t_1$. The 3D plots of the spectrum defined by Eq.(6.3) for several values of α are shown in Fig.6.2, while the 2D plots along highly-symmetric lines are represented in Fig.6.3. For $\alpha = 1$, near the three-band-touching points Γ and M, one observes almost flat middle bands [206]. These two middle bands support completely flat energy lines, which are extended over full BZ. Below we proceed with description of highly-symmetric points in terms of van Hove singularities in the DOS.

6.3 Spectrum structure around highly-symmetric points: van Hove singularities

Firstly, let us present general definitions that will be used throughout the text. By definition, the one-electron DOS per spin is given by

$$D(\varepsilon) = \sum_{i=1}^{4} \int_{BZ} \frac{d^2k}{(2\pi)^2} \delta\left[\varepsilon - \varepsilon_i(\mathbf{k})\right], \tag{6.5}$$

with i running over the band dispersions $\varepsilon_i(\boldsymbol{k})$ found from Eq.(6.3). Due to chiral symmetry the DOS is an even function of energy. The ordinary

VHS with the logarithmic diverging DOS occurs at saddle point $\boldsymbol{k}_s$ of a particular band in which

$$\nabla_{\mathbf{k}}\varepsilon(\mathbf{k}) = \mathbf{0} \text{ and } \det\mathcal{D} < 0, \tag{6.6}$$

where $\mathcal{D}_{ij} \equiv \frac{1}{2}\partial_i\partial_j\varepsilon(\mathbf{k})$ is the 2×2 Hessian matrix of a dispersion $\varepsilon(\mathbf{k})$ at $\boldsymbol{k}_s$. Here and below we use short-hand notation $\partial_i = \partial_{k_i}$. After proper rotation of a basis, the dispersion around saddle point can be conveniently represented as $\varepsilon - \varepsilon_s \approx -\zeta p_x^2 + \beta p_y^2$ with wave vector deviation $\mathbf{p} = \mathbf{k} - \mathbf{k}_s$. The two coefficients ζ and β are the eigenvalues of $\mathcal{D}$ and satisfy the condition $-\zeta\beta = \det\mathcal{D} < 0$.

The high-order VHS corresponds to saddle point with the following properties [25]:

$$\nabla_{\mathbf{k}}\varepsilon = \mathbf{0} \text{ and } \det\mathcal{D} = 0. \tag{6.7}$$

This class of VHS can be divided into two types: $\zeta = \beta = 0$ (multicritical VHS), or $\zeta \neq 0,\ \beta = 0$. The DOS is expected to have a power-law divergence at such points. The position of all VHS can be found by differentiating Eq.(6.3) and setting $\nabla_{\mathbf{k}}\varepsilon = 0$, from which we get the system of equations:

$$\begin{aligned} &\sin(ak_x)\left(\varepsilon - t_1\cos(ak_y)\right) = 0,\\ &\sin(ak_y)\left(\varepsilon - t_1\cos(ak_x)\right) = 0. \end{aligned} \tag{6.8}$$

Below we perform expansion of the energy spectrum of T-graphene around highly-symmetric points and flat lines and identify the corresponding VHS type with the DOS divergence.

6.3.1 Γ and M points

Before proceeding with calculation, we underline that previously mentioned symmetry of spectrum makes these two points equivalent up to change of energy sign. Thus, the analysis around the Γ point can be directly translated to the M point and vice versa by chiral symmetry.

To find the approximate expressions for band energies around highly-symmetric points, we perform the series expansion of spectral equation (6.3). We write $\varepsilon = \varepsilon_i^{(0)} + \delta$, with $\varepsilon_i^{(0)}$ is the energy of i-th band exactly at the given point in k-space. Then, we expand equation into series in δ and $\boldsymbol{k}a$ (measured from the given point), and find the solution for δ in

leading order. Performing this for Γ point, we find the following results in the case $\alpha > 1$:

$$\frac{\varepsilon_1}{t_1} \approx -1 - 2\alpha + \frac{\alpha|\boldsymbol{k}|^2 a^2}{4(\alpha+1)}, \tag{6.9}$$

$$\frac{\varepsilon_{2,3}}{t_1} \approx 1 - \frac{a^2\alpha}{4\left(\alpha^2-1\right)}\left[\alpha|\boldsymbol{k}|^2 \pm \sqrt{\left(\alpha^2|\boldsymbol{k}|^4 - 4(\alpha^2-1)k_x^2k_y^2\right)}\right], \tag{6.10}$$

$$\frac{\varepsilon_4}{t_1} \approx -1 + 2\alpha + \frac{\alpha|\boldsymbol{k}|^2 a^2}{4(\alpha-1)}. \tag{6.11}$$

The numbering of bands goes from the lower one to the upper one (for $\alpha < 1$ the indices 2 and 4 should be interchanged). From expression (6.9) one can conclude that spectrum of tight-binding Hamiltonian (6.2) is bounded by $-1-2\alpha < \varepsilon < 1+2\alpha$ at zero temperature. In particular, it follows from Eq.(6.10) that the top of band ε_3 has completely flat lines along k_x and k_y axes.

In the case $\alpha = 1$ we find the following expansions for three upper bands (which have triply degenerate point (see also Ref.[206])):

$$\frac{\varepsilon_1}{t_1} \approx -3 + \frac{1}{8}a^2|\boldsymbol{k}|^2,\ \frac{\varepsilon_3}{t_1} \approx 1 - \frac{k_x^2k_y^2a^2}{2|\boldsymbol{k}|^2},\ \frac{\varepsilon_{2,4}}{t_1} \approx 1 \pm \frac{a}{\sqrt{2}}|\boldsymbol{k}| - \frac{a^2\left(k_x^2-k_y^2\right)^2}{16|\boldsymbol{k}|^2}. \tag{6.12}$$

The two bands $\varepsilon_{2,4}$ form Dirac cones with Fermi velocity $v_F = at_1/\sqrt{2}\hbar$ with additional square-order corrections in $|\boldsymbol{k}|a$. The middle band ε_3 is completely flat in first-order approximation, but has nontrivial anisotropic corrections of second-order in $|\boldsymbol{k}|a$.

The Γ and M points define the energy boundaries of each band (see Fig.6.2). For $\alpha \leq 1$ the bands are in the ranges $[-1-2\alpha, -1]$, $[-1, -1+2\alpha]$, $[1-2\alpha, 1]$, $[1, 1+2\alpha]$ measured in units of t_1. It follows from the expansions (6.9)-(6.11) taken at $\boldsymbol{k} = 0$. We find that the gap near $\varepsilon = 0$ opens for $\alpha < 1/2$. For the $\alpha \geq 1$ the bands' energy ranges are $\varepsilon/t_1 \in [-1-2\alpha, 1-2\alpha]$, $[-1, 1]$ for both middle bands, and $[-1+2\alpha, 1+2\alpha]$. In this case the gaps are opened for $\alpha > 1$ above $\varepsilon = t_1$ and below $\varepsilon = -t_1$, respectively. These features of spectrum are manifested in vanishing DOS in corresponding gap energy ranges, see Fig.6.3.

Next, we identify the type of VHS at $\varepsilon_3 = t_1$ in $\alpha = 1$ case. For this purpose, we evaluate the DOS contribution for each band separately, taking the leading term in wavevector expansion. The integration over

wavevector in Eq.(6.5) is extended to cut-off parameter Λ of effective expansions (6.12). Then, the Dirac cones give the standard graphene-like result:

$$D_2(\varepsilon) + D_4(\varepsilon) = \frac{|\varepsilon - t_1|}{\pi a^2 t_1^2}. \tag{6.13}$$

The evaluation of DoS for middle nearly flat band is more complicated, but can be performed in polar coordinates:

$$D_3(\varepsilon \lesssim t_1) = \int_0^{\Lambda}\int_0^{2\pi} \frac{kdkd\phi}{(2\pi)^2}\delta\left[\varepsilon - t_1 + t_1\frac{k^2a^2\sin^2(2\phi)}{8}\right]. \tag{6.14}$$

We emphasize the fact that the middle band contributes only for $\varepsilon < t_1$ and the corresponding DOS is asymmetric. The integration over k is easily performed, and the integration over angle can be confined to first quadrant with adding a total factor 4. Then, one should integrate in the limits where the solutions under delta-function are possible $\phi_{min} < \phi < \phi_{max}$:

$$\phi_{min} = \frac{1}{2}\arcsin\left(\sqrt{\frac{8(1-\varepsilon/t_1)}{\Lambda^2 a^2}}\right),\ \phi_{max} = \frac{\pi}{2} - \frac{1}{2}\arcsin\left(\sqrt{\frac{8(1-\varepsilon/t_1)}{\Lambda^2 a^2}}\right). \tag{6.15}$$

Thus, the integral for DOS becomes

$$D_3(\varepsilon \lesssim t_1) = \frac{1}{t_1 a^2}\int_{\phi_{min}}^{\phi_{max}} d\phi \frac{4}{\sin^2(2\phi)} \approx \frac{2}{t_1 a}\frac{\Lambda}{\sqrt{2(1-\varepsilon/t_1)}}. \tag{6.16}$$

with the $1/\sqrt{1-\varepsilon/t_1}$ divergence, as was noted previously. This power-law divergence together with asymmetry of the DOS clearly indicates, that this point corresponds to high-order VHS (see middle peaks of the DOS in all panels of Fig.6.3). Below we show that this holds true for all points on flat lines in the dispersion $\varepsilon_3(\mathbf{k})$. Also one should note that this singularity has larger exponent $\kappa = 1/2$ (which is defined as $D_3(\varepsilon \le t_1) \sim |t_1 - \varepsilon|^{-\kappa}$) than in twisted bilayer graphene ($\kappa = 1/4$, [25]), and the same as in $Sr_3Ru_2O_7$ [217] and $\beta - YbAlB_4$ [218] materials.

Above we have found the long wavelength expansions of spectrum for small values of wavevector $\boldsymbol{k}$. However, these expansions are violated if the model parameter α approaches 1. In this case we can use another series expansion of the spectrum: we assume that $|1-\alpha| \sim |\boldsymbol{k}a|$ are of the

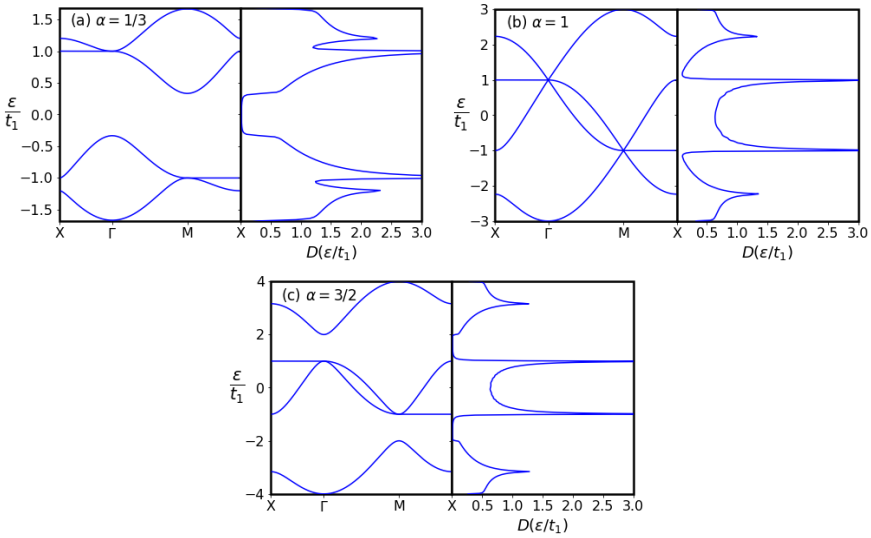

Figure 6.3. The spectrum of T-graphene along the closed path $X-\Gamma-M-X$ and DOS for $\alpha = 1/3$, 1 and $\alpha = 3/2$. DOS is plotted on the right of each spectrum, and is measured in units of $\frac{1}{a^2 t_1}$. DOS is regularized with finite broadening of levels, $\Gamma = 0.01 t_1$ to make plots smooth.

same order. Then, we replace both terms $|1-\alpha|$ and $|\boldsymbol{k}a|$ in Eq.(6.3) with $\zeta|1-\alpha|$ and $\zeta|\boldsymbol{k}a|$, respectively, and expand the obtained equation into powers of ζ. This guaranties that expansions keep contributions from both small values $|1-\alpha|$ and $|\boldsymbol{k}a|$ in the same leading order. Next, we solve the approximate spectral equation around each band, as for Eqs.(6.9)-(6.11), and set finally $\zeta = 1$, we find

$$\frac{\varepsilon_1}{t_1} = -1 - 2\alpha + \frac{(k_x^2+k_y^2)a^2}{8}, \quad \frac{\varepsilon_3}{t_1} = 1 - \frac{k_x^2 k_y^2 a^2}{2(k_x^2+k_y^2)},$$
$$\frac{\varepsilon_{2,4}}{t_1} = 1 - \left((1-\alpha) \pm \sqrt{\frac{(k_x^2+k_y^2)a^2}{2} + (1-\alpha)^2}\right). \tag{6.17}$$

The last two expressions show that the $|1-\alpha|$ competes with $|\boldsymbol{k}|a$ and their larger value defines the spectrum form in the leading order.

6.3.2 X-points and flat lines

At X point the eigenvalues of Hamiltonian (6.2) are

$$\varepsilon^X_{1,4} = \mp t_1\sqrt{1+4\alpha^2}, \quad \varepsilon^X_{2,3} = \mp t_1. \tag{6.18}$$

The energies $\varepsilon_{1,4}$ belong to lower and upper and bands, respectively, and the energies $\varepsilon_{2,3}$ belong to flat lines for the points in k-space, which are situated in the middle between band-touching points. In Appendix 6.6 we show how the flat lines are related to the C_4 point symmetry group of the lattice and structure of tight-binding Hamiltonian. Performing the series expansion of spectral equation in the same way as discussed above Eq.(6.9) but for wavevectors around $X = (0, \frac{\pi}{a})$, we find:

$$\varepsilon_1 \approx \varepsilon^X_1 + \frac{t_1 a^2}{4}\left[k_x^2\left(1+\frac{t_1}{\varepsilon^X_1}\right) - \left(k_y - \frac{\pi}{a}\right)^2\left(1-\frac{t_1}{\varepsilon^X_1}\right)\right], \tag{6.19}$$

$$\varepsilon_4 \approx \varepsilon^X_4 + \frac{t_1 a^2}{4}\left[k_x^2\left(1+\frac{t_1}{\varepsilon^X_4}\right) - \left(k_y - \frac{\pi}{a}\right)^2\left(1-\frac{t_1}{\varepsilon^X_4}\right)\right]. \tag{6.20}$$

These two dispersion relations represent ordinary VHS, defined via the conditions (6.6). The Hessian matrix is diagonal and its' elements are the derivatives of above dispersion relations with respect to wavevectors, $\mathcal{D} = \mathrm{diag}(\partial_{xx}\varepsilon, \partial_{yy}\varepsilon)$. The DOS exhibits a logarithmic divergence around $\varepsilon = \varepsilon^X_1$ and $\varepsilon = \varepsilon^X_4$: $D_{1,4}(\varepsilon) \sim \log\left(\frac{\Lambda a^2 t_1}{|\varepsilon - \varepsilon^X_{1,4}|}\right)$. These upper and lower peaks in DOS are clearly visible on Fig.6.3.

Next, we find the series expansion of $\varepsilon_{2,3}$ bands' dispersion around X point. Due to chiral symmetry mentioned after Eq.(6.3), it suffices to make expansion only for upper band, while for lower band it can be found by appropriate change of wavevectors. Expanding the spectral equation (6.3) for third band around energy $\varepsilon_3 = t_1$ into series in $k_x a$, we find:

$$\varepsilon_3 \approx t_1 - t_1\left[\frac{k_x^2 a^2}{2} - \frac{k_x^4 a^4}{4\alpha^2(1-\cos(k_y a))}\right]. \tag{6.21}$$

This approximation works well only for $\frac{k_x^4 a^4}{4\alpha^2(1-\cos(k_y a))} < \frac{k_x^2 a^2}{2}$, since this band has $\varepsilon_3 \leq t_1$ energy for all points in BZ. The Hessian matrix for the dispersion (6.21) has only one nonzero component on diagonal $\mathcal{D} = \mathrm{diag}\left(-\frac{t_1 a^2}{2}, 0\right)$. Thus, we observe that the middle bands at X-point and

in other points of flat line where $1-\cos(k_y a) \neq 1$ exhibit a high-order saddle point ($\det \mathcal{D} = 0$). One can check that the DOS for dispersion (6.21) has a inverse square root divergence $1/\sqrt{t_1 - \varepsilon}$ with energy, with benchmark asymmetry:

$$D_3(\varepsilon \lesssim t_1) = \int \frac{d^2k}{(2\pi)^2}\delta\left[\varepsilon - t_1\left(1 - \frac{k_x^2 a^2}{2}\right)\right] = \frac{\Lambda}{\sqrt{2}\pi^2 a t_1 \sqrt{1-\varepsilon/t_1}}. \tag{6.22}$$

In Fig.6.3 we present dispersion relations for T-graphene along the path $X-\Gamma-M-X$ which represents the main features in spectrum (left part of each panel) and DOS (regularized by finite level broadening, right part of each panel) for the values $\alpha = 1/3$, 1 and $\alpha = 3/2$. Note that the path length in $M-\Gamma$ direction is $\sqrt{2}$ times larger than that in $X-M$ or $\Gamma-X$ directions. Our plots show that at energies $\mp t_1\sqrt{1+4\alpha^2}$ DOS exhibits logarithmic divergences, which are the standard VHS at X points. At the same time, the much stronger peaks in DOS correspond to flat lines in spectrum at energies $\mp t_1$ which are 'high-order' VHS. Our results for spectra agree with the results of Refs.[204–206], however, the dispersion ε_3 in Eq.(6.12) was not recognized as the one exhibiting high-order VHS.

Fig.6.3 demonstrates also evolution of DOS as the function of the hopping parameter α. At $\varepsilon = 0$ we find that for $\alpha < 1/2$ there are no states (insulating phase), while for larger α the states are present. For energies $|\varepsilon| < t_1$ the DOS is always finite for $\alpha > 1/2$ meaning metallic behavior. On the other hand, for energies $|\varepsilon| > t_1$ and $\alpha > 1$ we observe the presence of gaps in the DOS.

In Sec.6.4 we will study the behavior of orbital susceptibility around van Hove singularities.

6.3.3 Effective models of band touching point: linear and quadratic approximations

In the tight-binding model of square-octagon lattice the band touching exists at two highly-symmetric points - Γ and M. Since they are related by chiral symmetry (see discussion after Eq.(6.3)), we need to build an effective Hamiltonian only at one of these points. As was proposed in Ref.[206], one can perform a rotation to C_{4v} basis utilizing the following

unitary matrix

$$U_{C_{4v}} = \frac{1}{2}\begin{pmatrix} 1 & \sqrt{2} & 0 & 1 \\ 1 & 0 & \sqrt{2} & -1 \\ 1 & -\sqrt{2} & 0 & 1 \\ 1 & 0 & -\sqrt{2} & -1 \end{pmatrix}, \tag{6.23}$$

which acts on four-component wave functions in sublattice space, defined below Eq.(6.2). After such unitary transformation we obtain the following first-order effective $SU(3)$ Hamiltonian near the Γ point:

$$H^{(1)}_{SU(3)} = t_1 \begin{pmatrix} 1 & 0 & -\frac{iak_x}{\sqrt{2}} \\ 0 & 1 & \frac{iak_y}{\sqrt{2}} \\ \frac{iak_x}{\sqrt{2}} & -\frac{iak_y}{\sqrt{2}} & 2\alpha - 1 \end{pmatrix}. \tag{6.24}$$

This Hamiltonian is useful for understanding how the Dirac cones emerge in spectrum for $\alpha = 1$. The spectrum defined by this Hamiltonian is

$$\frac{\varepsilon_0}{t_1} = 1, \quad \frac{\varepsilon_\pm}{t_1} = \alpha \pm \sqrt{\frac{a^2|\mathbf{k}|^2}{2} + (\alpha - 1)^2}, \tag{6.25}$$

where ε_0 corresponds to the ε_3 band of tight-binding model, and $\varepsilon_{-,+}$ to the bands $\varepsilon_{2,4}$ respectively. The corresponding eigenvectors are

$$\begin{aligned} \Psi_0 &= \frac{1}{|\boldsymbol{k}|}\left(k_y, k_x, 0\right), \\ \Psi_- &= \frac{(ik_x a, -ik_y a, \sqrt{2}(1-\varepsilon_-))}{\sqrt{2\left(|\boldsymbol{k}|^2 a^2 + 2(1-\alpha)(1-\varepsilon_-)\right)}}, \\ \Psi_+ &= \frac{(-ik_x a, ik_y a, \sqrt{2}(\varepsilon_+ - 1))}{\sqrt{2\left(|\boldsymbol{k}|^2 a^2 + 2(\alpha-1)(\varepsilon_+ - 1)\right)}}. \end{aligned} \tag{6.26}$$

One should note that the linear Hamiltonian of such type does not capture the spectral structure of middle band. Instead, the middle band is treated as completely flat, and the corresponding effective theory is an example of pseudospin-1 fermion models (see Ref.[229] for topological classification of such theories). Since the aim of present paper is to analyze the role of high-order VHS, we need to build the effective Hamiltonian that correctly captures the dispersion of middle band at leading order in $|\boldsymbol{k}|a$. The needed dispersion is presented, for example, in Eq.(6.12) in the $\alpha = 1$ case.

To find corresponding effective Hamiltonian, we use Löwdin method [230], which is also called Löwdin partitioning (the example calculation for Lieb-kagome Hamiltonian was performed in Ref.[231]). The idea is to perform the rotation of the full tight-binding Hamiltonian (6.2) via the unitary transformation (6.23), and then represent it in a block-like form:

$$H = \left(\begin{array}{c|c} H_{\alpha\alpha} & H_{\alpha\beta} \\ \hline H_{\beta\alpha} & H_{\beta\beta} \end{array}\right), \tag{6.27}$$

where the α subspace describes $SU(3)$ band-touching and β subspace corresponds to lower band, decoupled from other three bands by relatively large gap. Then, the effective second-order Hamiltonian around band-touching is written as

$$\mathcal{H}_\alpha = H_{\alpha\alpha} + H_{\alpha\beta}\left(\varepsilon_0 - H_{\beta\beta}\right)^{-1} H_{\beta\alpha}, \tag{6.28}$$

where $\varepsilon_0 = \varepsilon_{2,3}(\boldsymbol{k} = 0) = t_1$. For Γ point this Hamiltonian has the following form

$$H^{(2)}_{SU(3)} = \hat{\varepsilon}^{(0)} + t_1 \begin{pmatrix} -\frac{a^2(2\alpha+1)k_x^2}{4(\alpha+1)} & \frac{a^2 k_x k_y}{4(\alpha+1)} & -\frac{iak_x}{\sqrt{2}} \\ \frac{a^2 k_x k_y}{4(\alpha+1)} & -\frac{a^2(2\alpha+1)k_y^2}{4(\alpha+1)} & \frac{iak_y}{\sqrt{2}} \\ \frac{iak_x}{\sqrt{2}} & -\frac{iak_y}{\sqrt{2}} & \frac{\boldsymbol{k}^2 a^2}{4} \end{pmatrix}, \tag{6.29}$$

where $\hat{\varepsilon}^{(0)} = t_1 \mathrm{diag}(1,\, 1,\, 2\alpha - 1)$. Such simple Hamiltonian is particularly useful when the proper dispersion of all three bands is needed at leading order.

6.4 Orbital susceptibility

In this section we study the manifestation of T-graphene spectrum features considered above, in particular, VHS of both kinds, in the orbital susceptibility. The susceptibility measures the response of a electronic system to an external magnetic field and is defined standardly as the second derivative of the grand canonical potential at zero field. The main formula, which is most suitable in our case for numerical calculation, was given in Ref.[232], the more general formula was derived in Ref.[227]. The susceptibility can be represented as

$$\chi_{\mathrm{orb}}\,(\mu, T) = -\frac{\mu_0 e^2}{12\hbar^2}\frac{\mathrm{Im}}{\pi S}\int_{-\infty}^{\infty} n_{\mathrm{F}}(\varepsilon)\,\mathrm{Tr}\,\hat{X}\mathrm{d}\varepsilon. \tag{6.30}$$

Here $n_F(\varepsilon) = 1/(e^{(\varepsilon-\mu)/T}+1)$ is the Fermi distribution, $\mu_0 = 4\pi \times 10^{-7}$ in SI units and S is the area of the sample. The operator $\hat{X}$ is written in terms of zero-field Green function $G(\boldsymbol{k})$ and Bloch Hamiltonian $H(\boldsymbol{k})$, and $\partial_{x,y}$ are partial derivatives over momenta:

$$\hat{X} = G(\boldsymbol{k})\partial_x^2 H(\boldsymbol{k})G(\boldsymbol{k})\partial_y^2 H(\boldsymbol{k}) - G(\boldsymbol{k})\partial_{xy}^2 H(\boldsymbol{k})G(\boldsymbol{k})\partial_{xy}^2 H(\boldsymbol{k}) + \\ + 2\left([G(\boldsymbol{k})\partial_x H(\boldsymbol{k}), G(\boldsymbol{k})\partial_y H(\boldsymbol{k})]\right)^2. \tag{6.31}$$

The trace operation contains the integral over the BZ and the trace over band indices:

$$\mathrm{Tr}(\bullet) = \sum_k \mathrm{tr}(\bullet) = S\int_{\mathrm{BZ}} \frac{\mathrm{d}^2k}{4\pi^2}\,\mathrm{tr}(\bullet). \tag{6.32}$$

The orbital susceptibility can be rewritten in several other forms, one of them without commutator [227],

$$\chi_{\mathrm{orb}}(\mu,T) = -\frac{\mu_0 e^2}{12\hbar^2}\frac{\mathrm{Im}}{\pi S}\int_{-\infty}^{+\infty} n_F(\varepsilon)\,\mathrm{Tr}\left\{GH^{xx}GH^{yy} \right. \\ \left. - GH^{xy}GH^{xy} - 4\left(GH^xGH^xGH^yGH^y - GH^xGH^yGH^xGH^y\right)\right\}\mathrm{d}\varepsilon. \tag{6.33}$$

Here $G = G(\boldsymbol{k})$ is the Green function and H^i, H^{ij} denote the first and second derivatives of Hamiltonian with respect to components of momenta $k_{i,j}$ and the trace contains momenta integration, as defined in Eq. (6.32). The last formula can be also rewritten [227] in terms of previously found one by Gomez-Santos [226],

$$\chi_{\mathrm{orb}}(\mu,T) = -\frac{\mu_0 e^2}{2\hbar^2}\frac{\mathrm{Im}}{\pi S}\int_{-\infty}^{+\infty} n_F(\varepsilon)\,\mathrm{Tr}\left\{GH^xGH^yGH^x \right. \\ \left. \times\, GH^y + \frac{1}{2}\left(GH^xGH^y + GH^yGH^x\right)GH^{xy}\right\}\mathrm{d}\varepsilon. \tag{6.34}$$

Here the first term represents the Fukuyama result [233]. Three formulas for susceptibility are equivalent of course, and the use of a specific formula depends on possible simplifications, for example, for Hamiltonians linear in momenta the expressions (6.31) or (6.33) are preferred since the terms with second derivatives H^{ij} vanish.

To check the numerical results below we use the sum rule which states that the integral of the orbital susceptibility over the whole band vanishes:

$$\int \chi_{\mathrm{orb}}(\mu,T)d\mu = 0. \tag{6.35}$$

The derivation of the sum rule for general tight-binding model was given in Ref.[13]. Below we apply the formulas for orbital susceptibility to particular models, namely - tight-binding model of tetragraphene and effective low-energy $SU(3)$ models.

6.4.1 Application of general formulas to tetragraphene

Let us now apply the formula (6.30) to tetragraphene Hamiltonian (6.2). Since the second derivatives $\partial^2_{xy}H$ and $\partial^2_{yx}H$ vanish, the operator $\hat{X}$ reduces to

$$\hat{X} = G(\boldsymbol{k})\partial_x^2 H(\boldsymbol{k})G(\boldsymbol{k})\partial_y^2 H(\boldsymbol{k}) + 2\left([G(\boldsymbol{k})\partial_x H(\boldsymbol{k}), G(\boldsymbol{k})\partial_y H(\boldsymbol{k})]\right)^2. \tag{6.36}$$

The Green's function is given in Appendix 6.7. Then, calculating the trace of $\hat{X}$ for each term separately, we find the expressions presented in Appendix by Eqs.(6.59) and (6.60). We denote the first term with second derivatives in (6.36) as "*term 1*" and the term with commutator as "term 2". Here and thereafter we use dimensionless energy parameter $\varepsilon \to \varepsilon/t_1$ to simplify the form of expressions. One should notice that the numerators in both terms (6.59) and (6.60) are real, thus the imaginary part comes fully from integration over energy due to the presence of singular denominators. We write the determinants as $\prod_{i=1}^{4}(\varepsilon - \varepsilon_i(\boldsymbol{k}))$, where $\varepsilon_i(\boldsymbol{k})$ are band energies measured in units of t_1.

One can use also an alternative expression (6.34) for susceptibility obtaining shorter expression

$$\chi_{\rm orb}(\mu, T) = -\frac{\mu_0 e^2 t_1}{2\hbar^2}\frac{\rm Im}{\pi}\int\limits_{-\infty}^{+\infty} d\varepsilon n_F(t_1\varepsilon)\int\limits_{BZ}\frac{d^2k}{4\pi^2}\,{\rm tr}\left\{GH^xGH^yGH^xGH^y\right\}. \tag{6.37}$$

Evaluating the trace, we find

$${\rm tr}\left\{GH^xGH^yGH^xGH^y\right\} = \left(\frac{2\alpha a(\varepsilon^2-1)}{\det[\varepsilon - \frac{1}{t_1}H(\boldsymbol{k})]}\right)^4 \sin^2(k_x a)\sin^2(k_y a). \tag{6.38}$$

The advantage of this formula is that the numerator is much simpler comparing to Eqs.(6.59)-(6.60). However, the larger power of denominator

makes it harder to perform numerical calculation, since the behavior at band-touching point is more singular.

The integrals over energy can be evaluated analytically using Cauchy formula with residues. Next, we need to calculate the integrals over wavevector in full BZ. They are cumbersome and can be performed only numerically.

The numerical evaluation can be performed by sampling many points in BZ, and replacing integral by a quadrature sum. For this purpose we use Monte Carlo approach - it converges very fast with increasing number of sample points for multidimensional integrals. Taking N sample points in BZ, the integral over d^2k is replaced by the sum $\int_{BZ} \frac{d^2k}{(2\pi)^2} f(\boldsymbol{k}) = \frac{1}{N}\sum_j f(\boldsymbol{k}_j)$. Then, the final formula used in evaluation is

$$\chi_{\text{orb}}\,(\mu,T) = \frac{\chi_0}{N}\sum_{j=1}^{N}\left[\sum_i \operatorname*{res}_{\varepsilon=\varepsilon_i} n_F(t_1\varepsilon) f^R(\varepsilon)\right]_{\boldsymbol{k}=\boldsymbol{k}_j}. \tag{6.39}$$

The residues were evaluated analytically using expressions (6.59)-(6.60), and the band energy solutions of spectral equation (6.3) were substituted numerically into final expressions. Here we introduced the scale factor for susceptibility $\chi_0 = \mu_0 e^2 a^2 t_1/12\hbar^2$.

The results of evaluation for χ as a function of chemical potential are shown in Fig.6.4. We have checked that good convergence is reached for $N = 10^5$ and $N = 5\times 10^5$ for the terms (6.59) and (6.60), respectively. The errors of integration become in this case several orders less than the absolute values of susceptibility. As a test, we checked that the sum rule, which is given by Eq.(6.35), holds true with the same precision.

The orbital susceptibility exhibits standard weak diamagnetic peaks near the edges of the spectrum, which can be easily understood from the Landau-Peierls (LP) formula [227, 232, 234, 235],

$$\chi_{\text{LP}}(\mu,T) = \frac{\mu_0 e^2}{12\hbar^2}\sum_{i=1}^{4}\int \frac{d^2k}{4\pi^2} n'_F(\varepsilon_i)\left(\partial_x^2\varepsilon_i\partial_y^2\varepsilon_i - \partial_{xy}^2\varepsilon_i\partial_{xy}^2\varepsilon_i\right), \tag{6.40}$$

which takes into account only intraband contributions. Here $n'_F(\varepsilon)$ is a derivative of the Fermi distribution function. We note that the LP contribution in total susceptibility comes from the first two terms in Eq.(6.31) which contain second derivatives.

In the case of T-graphene only the lower (upper) band gives strong contribution to the orbital susceptibility at the lower (upper) edge of the

spectrum. This can be clearly seen from Figs.6.2 and 6.3, since at lower (upper) edge the corresponding band in Γ (M) point is separated by a large gap from other three bands. The dispersion of this band is quadratic in momenta, see Eq.(6.9), and both derivatives in first term of LP formula are positive. The second term exactly vanishes, and thus the LP susceptibility is negative because $n'_F(\varepsilon) < 0$. These peaks are clearly visible in susceptibility described by the red line (term 1) in panels a) - c) of Fig.6.4 (leftmost and rightmost negative peaks). At the same time, the Landau-Peierls formula does not capture the contribution of high-order saddle points. This is because the large contribution from a Fermi function derivative $n_F^{'}(\varepsilon_i)$ is compensated by vanishing determinant of Hessian matrix that is present in round brackets.

At the ordinary van Hove points, which are placed on upper and lower bands at X-points at the energy levels $\varepsilon^X_{1,4} = \mp\sqrt{1+4\alpha^2}$, one finds strong paramagnetic peaks. These peaks are also well-described by the Landau-Peierls formula (6.40). Substituting series expansion (6.19) or (6.20), one finds that only the first term in Landau-Peierls formula is nonzero, and have positive sign due to opposite signs of ∂_x^2 and ∂_y^2 derivatives. Moreover, due to the divergent DOS at this energy level, the contribution of this band dominates and leads to strong paramagnetism. This is also related to famous magnetic breakdown phenomena [234], where the quasiclassical approximation in terms of electronic orbits fails in the vicinity of saddle points due to effects of tunneling from one trajectory to the neighboring one that leads to rotation of the electron in a direction opposite to the direction of classical rotation (see Ref.[50] for physical picture of this phenomenon). Large paramagnetic peaks coming from the Landau-Peierls formula are well seen in the red line (term 1) in the left panel of Fig.6.4 ($\alpha = 1/3$). Due to the sum rule (6.35) they are almost compensated by diamagnetic contribution in the green line (term 2). The competition of two terms in Eq.(6.36) leads to several dia- to paramagnetic transitions when we continuously change the chemical potential μ (see Fig.6.4). The susceptibility for $\alpha = 3/2$ behaves qualitatively similar to the case with $\alpha = 1/3$.

The behavior of the susceptibility is more interesting when the hopping parameter α is close to unity. At the Fermi level $\mu = 0$ the orbital susceptibility does not exhibit any peculiar properties. However, when the doping is tuned to band-touching point $\mu = t_1$, one can expect nontrivial behavior of susceptibility due to presence of massless fermions forming a

Dirac cone and flat lines with high-order VHS of DOS. Near the energy levels $\mu = \pm t_1$ (see the panels b) and d) in Fig.6.4) we find strong diamagnetic and paramagnetic peaks. Since the contribution of high-order VHS is suppressed in the LP formula (term 1) we are left with diamagnetic contribution from the term 2 due to Dirac excitations when $|\mu| \gtrapprox t_1$. On the other hand, when $|\mu| \lessapprox t_1$ there is a strong paramagnetic contribution in the term 2 from high-order VHS. The existence of the orbital paramagnetism is a necessary condition to cancel the diamagnetic contribution in order to satisfy the sum rule (6.35). The competition of these two contributions leads to a sharp dia- to paramagnetic transition at $|\mu| \approx t_1$ (see panels b), d) in Fig.6.4. This transition manifests itself in Fig.6.5 where the susceptibility at $\mu = t_1$ is plotted as a function of α (blue line).

Below we analyze the orbital susceptibility for effective linear and quadratic Hamiltonians given by Eqs.(6.24) and (6.29) to obtain some insights into the physics of these peculiar features.

6.4.2 Analytical results in effective pseudospin-1 model around band-touching

Let us firstly use the linear effective Hamiltonian around band-touching point to find an analytical approximation for the susceptibility. It is given by Eq.(6.24), and we omit the dimensional parameter t_1, restoring it in the final expressions for susceptibility,

$$H_3 \equiv \frac{H_{SU(3)}}{t_1} = \begin{pmatrix} 1 & 0 & -\frac{iak_x}{\sqrt{2}} \\ 0 & 1 & \frac{iak_y}{\sqrt{2}} \\ \frac{iak_x}{\sqrt{2}} & -\frac{iak_y}{\sqrt{2}} & 2\alpha - 1 \end{pmatrix}. \tag{6.41}$$

The corresponding Green's function is

$$G_{SU(3)} = \frac{1}{\det[\varepsilon - H_3]} \times \begin{pmatrix} \varepsilon^2 - \frac{a^2k_y^2}{2} - 2\alpha(\varepsilon-1) - 1 & -\frac{1}{2}a^2k_xk_y & -\frac{ia(\varepsilon-1)k_x}{\sqrt{2}} \\ -\frac{a^2k_xk_y}{2} & \varepsilon^2 - \frac{a^2k_x^2}{2} - 2\alpha(\varepsilon-1) - 1 & \frac{ia(\varepsilon-1)k_y}{\sqrt{2}} \\ \frac{ia(\varepsilon-1)k_x}{\sqrt{2}} & -\frac{ia(\varepsilon-1)k_y}{\sqrt{2}} & (\varepsilon-1)^2 \end{pmatrix}. \tag{6.42}$$

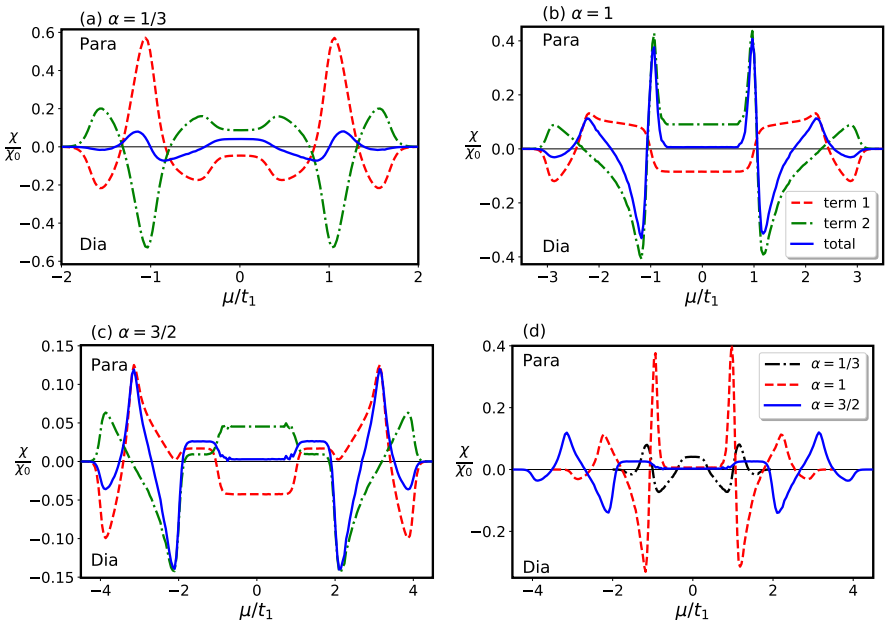

Figure 6.4. The dependence of susceptibility χ on chemical potential μ, measured in units of t_1 hopping parameter, for three values of α: a) 1/3, b) 1, c) 3/2. The susceptibility is normalized to scale factor $\chi_0 = \mu_0 e^2 a^2 t_1/12\hbar^2$. The legend on panel (b) shows the lines definitions in panels a) - c): dashed and dash-dotted lines correspond to first and second term contributions in $\hat{X}$ (see Eq.(6.36)), while the solid line describes the total susceptibility (the different ranges in y-axis are taken for better visibility). Panel d) shows the total susceptibility for three values of α.

The determinant in denominator is simple

$$\det[\varepsilon - H_3] = \frac{1-\varepsilon}{2}\left(a^2\boldsymbol{k}^2 + 2(\varepsilon-1)(2\alpha-\varepsilon-1)\right) \tag{6.43}$$

and gives two Dirac cones and the flat band at $\varepsilon = 1$. The first derivatives of Hamiltonian are,

$$H_3^x = \frac{a}{\sqrt{2}}\begin{pmatrix} 0 & 0 & -i \\ 0 & 0 & 0 \\ i & 0 & 0 \end{pmatrix},\ H_3^y = \frac{a}{\sqrt{2}}\begin{pmatrix} 0 & 0 & 0 \\ 0 & 0 & i \\ 0 & -i & 0 \end{pmatrix}, \tag{6.44}$$

while all second derivatives are zero. Then, we can apply the formula (6.34), which in our case reduces to

$$\chi_{\rm orb}(\mu,T) = -\frac{\mu_0 e^2 t_1}{2\hbar^2}\frac{\operatorname{Im}}{\pi S}\int\limits_{-\infty}^{+\infty} n_F(\varepsilon)\operatorname{Tr}\left\{GH^xGH^yGH^xGH^y\right\}\mathrm{d}\varepsilon. \tag{6.45}$$

Calculating the matrix trace we come at the orbital susceptibility given by the triple integral,

$$\begin{aligned}\chi_{\rm orb}(\mu,T) = -\frac{\mu_0 e^2 t_1}{2\hbar^2}\frac{\operatorname{Im}}{\pi}\int_{-\infty}^{+\infty} n_F(t_1\varepsilon)d\varepsilon \\ \times\int\frac{d^2k}{4\pi^2}\frac{16a^8k_x^2k_y^2}{\left(a^2\left(k_x^2+k_y^2\right)+2(\varepsilon-1)(2\alpha-\varepsilon-1)\right)^4}.\end{aligned} \tag{6.46}$$

The integration over momenta is easily performed using polar coordinates

$$\begin{aligned}&\int\frac{d^2k}{4\pi^2}\frac{16a^8k_x^2k_y^2}{\left(a^2\left(k_x^2+k_y^2\right)+2(\varepsilon-1)(2\alpha-\varepsilon-1)\right)^4} \\ &= \frac{a^2}{12\pi}\times\begin{cases}\frac{1}{2(\alpha-1)}\left(\frac{1}{\varepsilon-1}-\frac{1}{\varepsilon+1-2\alpha}\right), & \alpha\neq 1,\\ -\frac{1}{(\varepsilon-1)^2}, & \alpha = 1.\end{cases}\end{aligned} \tag{6.47}$$

Then, using the formula

$$\operatorname{Im}\int_{-\infty}^{+\infty}\frac{f(E)}{(E-\alpha)^j}\mathrm{d}E = -\frac{\pi}{(j-1)!}f^{(j-1)}(\alpha), \tag{6.48}$$

for susceptibility we finally obtain:

$$\chi_{\rm orb}(\mu,T) = -\frac{\chi_0}{2\pi}\begin{cases}\frac{1}{2(\alpha-1)}\left(n_F(t_1(2\alpha-1))-n_F(t_1)\right), & \alpha\neq 1,\\ t_1 n_F'(t_1), & \alpha = 1.\end{cases} \tag{6.49}$$

Note that the case $\alpha = 1$ is the limit of the upper case with $\alpha \neq 1$. The result for $\alpha = 1$ has the same functional structure as the susceptibility for low-energy model of graphene [227], but differs in numerical factor and sign. The latter difference is connected with the presence of flat band in spectrum. In such a case the flat band plays the crucial role giving strong delta-like paramagnetic response of the system at $\mu = t_1$ instead of diamagnetic, which was a result of two Dirac cones in graphene. Note however, that the linear effective Hamiltonian does not capture the correct dispersion of the middle band. The model contains completely flat band and the spectrum (6.25) is similar to a gapped dice model where the paramagnetic contribution from flat band exceeds diamagnetic contribution from Dirac cones (see Ref.[196])

The plot of effective susceptibility defined by Eq.(6.49) is shown in Fig.6.5 as a function of a hopping parameter α. On the plot it is denoted as "Eq.(24)" effective theory. We compare its dependence on α with total susceptibility of actual model evaluated numerically. The doping level $\mu = t_1$ coincides with the band touching point at which the high-order VHS and Dirac point are present for $\alpha = 1$. The numerical calculations demonstrate the presence of dia- to paramagnetic transition at $\alpha \approx 0.94$, which is absent in the low-energy result (6.49). Thus, we should analyze more precise effective model, which is given by the second-order Hamiltonian Eq.(6.29).

6.4.3 Paramagnetic-diamagnetic phase transition at band-touching point and second-order effective Hamiltonian

The calculation of orbital susceptibility for the second-order effective Hamiltonian (6.29) involves all terms in $\hat{X}$ operator (6.31), because all first and second derivatives of Hamiltonian (6.29) over k_i are nonzero. The corresponding Green's function is presented in Appendix, see Eq.(6.61). Since the calculations quickly become cumbersome, we present only numerical results here. For the integrals over wave number $\boldsymbol{k}$ we use Monte-Carlo method. The energies for each point in k-space are found from Eq.(6.63) and then we use the integration formula (6.39) multiplied by volume factor $\Lambda^2 a^2/\pi^2$. Here Λ is a cut-off parameter, that defines the region of applicability of second-order effective Hamiltonian (6.29). We estimated it as $\Lambda \approx 0.8\frac{1}{a}$ by comparing exact spectrum with one obtained from Eq.(6.63).

The orbital susceptibility for the effective Hamiltonian (6.29) at the

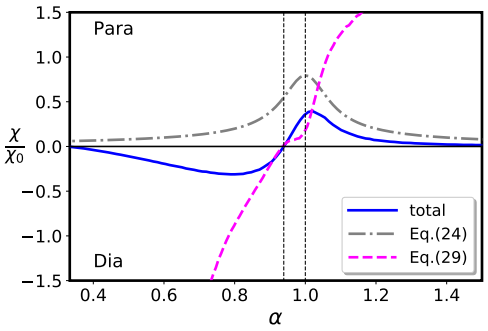

Figure 6.5. The dependence of orbital susceptibility on relative strength of tight-binding parameters $\alpha = t_2/t_1$ for $\mu = 1.0t_1$ and $T = 0.05t_1$. The numerically-evaluated total susceptibility (solid blue line) is compared with susceptibility obtained from effective pseudospin-1 Hamiltonians (6.24) (gray dash-dotted line) and (6.29) (magenta dashed line).

band-touching point $\mu = 1.0t_1$ as a function of a hopping parameter α is presented in Fig.6.5. It is clearly seen that this Hamiltonian exhibits dia- to paramagnetic transition at $\alpha = 0.94$ in agreement with tight-binding Hamiltonian and in contrast to the linear effective Hamiltonian (6.24). Qualitatively, one can expect that such a transition occurs due to the presence of Dirac cones, which give strong diamagnetism in graphene [197, 227], and the proximity of a high-order VHS that should result in strong paramagnetism. The competition between these two opposite responses together with the weak role of fourth band leads to a dia- to paramagnetic transition.

6.4.4 The role of van Hove singularities

Let us discuss the role of van Hove singularities in T-graphene. For the ordinary VHS the orbital susceptibility exhibits paramagnetic peak [50]. This can be understood using the standard Landau-Peierls formula for contribution of single band [227]. In T-graphene, at the doping level $\mu = \pm t_1$, one meets the three-band-touching points, at which two Dirac cones and middle band with flat lines intersect. In a single-layer graphene the presence of Dirac cones leads to singular diamagnetic contribution into orbital susceptibility $\chi \sim -\chi_0\delta(\mu)$ at zero temperature [197]. In the gapped dice model, spectrum of which is similar to (6.25), the paramagnetic contribution due to a flat band exceeds diamagnetic contribution

from Dirac cones (see Ref.[196]). In the case of T-graphene, the presence of middle band, which is not flat anymore but contains flat lines with high-order VH singularities on it, leads to strong paramagnetic contribution competing with diamagnetic contribution from Dirac cones, thus resulting in sign change of the orbital susceptibility.

High-order Van Hove singularities manifest themselves in many physical quantities as was reported in, e.g., Refs. [27, 28, 216–224]. In the present paper we focused on the magnetic susceptibility of non-interacting electrons in square-octagon lattice. However, one should expect the manifestation of high-order VHS of T-graphene also in other physical quantities besides orbital susceptibility which is a subject for future studies. We note that the accessibility of doping levels beyond the van Hove singularity was demonstrated in recent experiment for single-layer graphene [236].

6.5 Conclusions

In this paper we have studied the spectrum structure of tight-binding model for square-octagon lattice and analyzed the emergence of Dirac cones and van Hove singularities of different type. Firstly, we found that the singularities in DOS, that correspond to the flat lines in spectrum of T-graphene, represent VHS of high-order. Their benchmarks are large divergence exponent $\kappa = 1/2$ (instead of logarithmic divergence for ordinary VHS) and asymmetry of DOS near corresponding energy level. Such high-order saddle points in spectrum are intermediate between the ordinary saddle points and completely flat bands. Also, using the Löwdin partitioning, we derived an effective second-order Hamiltonian that correctly captures dispersions of three bands near the high-order saddle point.

Secondly, we have studied the orbital susceptibility of electrons on square-octagon lattice. We have found that while for ordinary VHS there are standard paramagnetic peaks predicted long ago by Vignale [50], the recently introduced high-order VHS [25] manifest themselves in a more complicated way. The tight-binding magnetic susceptibility exhibits several dia- to paramagnetic transitions when a chemical potential runs the whole zone.

Studying the orbital susceptibility at band-touching point ($\mu = t_1$) as a function of the tight-binding hoppings ratio α, we found a dia- to paramagnetic transition at $\alpha \approx 0.94$. Its existence can be qualitatively understood due to competitions of contributions from Dirac cones, which

give strong diamagnetism, and high-order VHS that result in strong paramagnetism. The effective low-energy pseudospin-1 Hamiltonian near the Γ point (6.24) correctly describes paramagnetic contribution but does not capture the dia- to paramagnetic transition. On the other hand, the effective Hamiltonian (6.29), which keeps second-order terms in a wavevector expansion, correctly reproduces the dia- to paramagnetic transition at $\alpha = 0.94$ given by the tight-binding Hamiltonian.

The tight-binding parameter α can be varied due to in-plane deformations keeping C_4 symmetry, thus allowing to verify the dia- to paramagnetic transition in experiment. Though it is not probably easy to fine-tune the hopping parameters experimentally, one can observe the different phases by analyzing different materials that are based on square-octagon lattice (see Refs. [53, 211]). Also, the T-graphene model can be realized experimentally with cold fermionic atoms in an optical lattice, or in phononic crystals [237]. In these cases it could be possible to test directly the sign change of the susceptibility as a function of α. In further studies of the T-graphene model it would be interesting to include impurities and interactions. In the recent publication [238] the role of high-order VHS in the orbital magnetic susceptibility was studied for twisted bilayer graphene. These studies complement the analysis in the present work.

6.6 Appendix: Flat lines in dispersion of middle bands and lattice symmetry

In this Appendix we show that the flat lines in spectrum are related to the C_4 point symmetry group. Also we show, that every point of flat line represents a high-order saddle point. Firstly, one can check that setting $k_x = 0$ (or $k_y = 0$) in spectral equation (6.3), it can be factorized:

$$(\varepsilon - 1)\left(-\left(4\alpha^2 + 1\right)\varepsilon + 4\alpha^2 \cos(ak_y) + \varepsilon^3 + \varepsilon^2 - 1\right) = 0. \qquad (6.50)$$

Here we used scaled energy parameter ε, measured in units of t_1. Thus, we find the middle band dispersion $\varepsilon = 1$, which describes a flat line. The same property of spectral equation holds true for $k_x a = \pm\pi$ and $k_y a = \pm\pi$ lines, with $\varepsilon = -1$.

The wavevector in tight-binding Hamiltonian (6.2) is measured from Γ point. Performing the rotation to the basis of C_4 symmetry group via the

unitary matrix given in Eq.(6.23), we find the transformed Hamiltonian $U^{\dagger}_{C_{4v}} H U_{C_{4v}}$. Along flat line direction $k_x = 0$ (and similarly for $k_y = 0$) the Hamiltonian reduces to the matrix

$$U^{\dagger}_{C_{4v}} H U_{C_{4v}}(k_x = 0, k_y) = \frac{t_1}{2} \times \begin{pmatrix} -1 - 4\alpha - \cos(ak_y) & 0 & i\sqrt{2}\sin(ak_y) & -1 + \cos(ak_y) \\ 0 & 2 & 0 & 0 \\ -i\sqrt{2}\sin(ak_y) & 0 & 2\cos(ak_y) & i\sqrt{2}\sin(ak_y) \\ -1 + \cos(ak_y) & 0 & -i\sqrt{2}\sin(ak_y) & -1 + 4\alpha - \cos(ak_y) \end{pmatrix}. \tag{6.51}$$

Thus, one can conclude that the presence of flat lines is protected not only by C_4 symmetry, but also by the geometry of tight-binding model. As was noted in Ref.[206], at the Γ point the flat lines represent nearly flat band (two lines intersect at the angle $\frac{\pi}{2}$). When the two hopping parameters are equal, $\alpha = 1$, the corresponding linear low-energy model (6.24) treats the middle band as completely flat and is similar to a pseudospin-1 model. However, in the second order approximation (see Eq.(6.29)) the middle band becomes dispersive. This fact distinguishes this pseudospin-1 model from other models, such as Lieb [21], Kagome [75] or $\alpha - T_3$ [13, 14, 89] models, where the presence of exactly flat band is supported by the lattice geometry in tight-binding approximation.

Finally, expanding the spectral equation (6.3) near the flat line $k_x = 0$ up to second order in $k_x a$, we find

$$\delta^4 - 4\delta^3 + 4\left(1 - \alpha^2\right)\delta^2 + 2\alpha^2\delta\left((k_x a)^2 - 2\cos(k_y a) + 2\right) + 2\alpha^2 (k_x a)^2 (\cos(k_y a) - 1) = 0. \tag{6.52}$$

Here $\delta = 1 - \varepsilon$ measures the deviation of energy from flat line value. In this equation we can omit the third and fourth order corrections (δ^3 and δ^4), and obtain simple quadratic equation. The solution, that corresponds to the flat line, has the following approximate behavior

$$\delta \approx \frac{k_x^2 a^2}{2} - \frac{k_x^4 a^4}{4\alpha^2 (\cos(k_y a) - 1)}. \tag{6.53}$$

The determinant of Hessian matrix for such a solution is always zero. Thus we conclude, that every point on a flat line is a high-order saddle point.

6.7 Appendix: Green's function of tight-binding and Löwdin Hamiltonians

In this Appendix we calculate the Green function of the tight-binding Hamiltonian (6.2). Standardly it is defined as

$$G(\boldsymbol{k},\varepsilon)=\frac{1}{t_1}\left(\varepsilon-\frac{1}{t_1}H(\boldsymbol{k})\right)^{-1} \tag{6.54}$$

for energy ε measured in units of t_1. Using the formula for adjoint matrix, we find the simple but long expression. For the clarity, we write the Green's function in block form:

$$G(\boldsymbol{k},\varepsilon)=\frac{1}{t_1\det[\varepsilon-\frac{1}{t_1}H(\boldsymbol{k})]}\begin{pmatrix} G_{11} & G_{12}\\ G_{12}^{\dagger} & G_{22}\end{pmatrix}. \tag{6.55}$$

The corresponding blocks are given by the following expressions:

$$G_{11}(\boldsymbol{k},\varepsilon)= \tag{6.56}$$
$$\begin{bmatrix} \varepsilon(-2\alpha^2+\varepsilon^2-1)+2\alpha^2\cos k_y a & \alpha e^{-ik_y a}(-\varepsilon+e^{ik_x a})(-1+\varepsilon e^{ik_y a})\\ \alpha e^{-ik_x a}(-1+\varepsilon e^{ik_x a})(-\varepsilon+e^{ik_y a}) & \varepsilon(-2\alpha^2+\varepsilon^2-1)+2\alpha^2\cos k_x a\end{bmatrix},$$

$$G_{12}(\boldsymbol{k},\varepsilon)= \tag{6.57}$$
$$\begin{bmatrix} 2\alpha^2(\varepsilon-\cos k_y a)-(\varepsilon^2-1)e^{ik_x a} & \alpha(-\varepsilon+e^{ik_x a})(\varepsilon-e^{ik_y a})\\ \alpha(-\varepsilon+e^{ik_x a})(\varepsilon-e^{ik_y a}) & 2\alpha^2(\varepsilon-\cos k_x a)-(\varepsilon^2-1)e^{ik_y a}\end{bmatrix},$$

$$G_{22}(\boldsymbol{k},\varepsilon)= \tag{6.58}$$
$$\begin{bmatrix} \varepsilon(-2\alpha^2+\varepsilon^2-1)+2\alpha^2\cos k_y a & \alpha e^{-ik_x a}(-1+\varepsilon e^{ik_x a})(-\varepsilon+e^{ik_y a})\\ \alpha e^{-ik_y a}(-\varepsilon+e^{ik_x a})(-1+\varepsilon e^{ik_y a}) & \varepsilon(-2\alpha^2+\varepsilon^2-1)+2\alpha^2\cos k_x a\end{bmatrix}.$$

These expressions are used to evaluate the traces for "*term 1*" and "*term 2*" (first and second terms in Eq.(6.36)):

$$\begin{aligned}&\mathrm{tr}\,[\text{term 1}]=\frac{a^4}{\det[\varepsilon-\frac{1}{t_1}H(\boldsymbol{k})]^2}\times\\ &\Big[4\alpha^2\left(\left(\varepsilon^2+1\right)\cos(k_x a)-2\varepsilon\right)\left(\left(\varepsilon^2+1\right)\cos(k_y a)-2\varepsilon\right)\Big],\end{aligned} \tag{6.59}$$

$$\begin{aligned}
&\mathrm{tr}\,[\text{term 2}] = \frac{16\alpha^2 a^4}{\det[\varepsilon - \frac{1}{t_1}H(\boldsymbol{k})]^3}\times \\
&\Big[t_1^2\alpha^2\left(\varepsilon^2+2\right)^2 + 2\alpha^2\varepsilon^2\cos(2k_y a)(\varepsilon\cos(k_x a)-1)^2 + \\
&+\varepsilon\left(\alpha^2\varepsilon\left(\varepsilon^2+2\right)\cos(2k_x a) + \left((\varepsilon^2-1)^2 - 4\varepsilon^2\alpha^2\left(\varepsilon^2+2\right)\right)\cos(k_x a)\right) \\
&+\cos(k_y a)\left(-2\left(2\alpha^2+1\right)\varepsilon^3 - 8\alpha^2\varepsilon - 4\alpha^2\varepsilon^3\cos(2k_x a)\right. \\
&+\left.\left(4\alpha\varepsilon-\varepsilon^2+1\right)\left(4\alpha\varepsilon+\varepsilon^2-1\right)\cos(k_x a) + \varepsilon^5 + \varepsilon\right) - \varepsilon^2\left(\varepsilon^2-1\right)^2\Big].
\end{aligned} \tag{6.60}$$

For the second-order effective Hamiltonian (6.29), which is obtained with the help of Löwdin partitioning method, the Green's function is (we set $a=1$ to simplify the notation)

$$G = \frac{1}{t_1 \det\left[\varepsilon - \frac{H^{(2)}_{SU(3)}(\boldsymbol{k})}{t_1}\right]}\times \tag{6.61}$$

$$\begin{pmatrix}
G_{11} & -\frac{k_x k_y\left(\boldsymbol{k}^2+16\alpha-4\varepsilon+4\right)}{16(\alpha+1)} & -\frac{ik_x\left(2(\varepsilon-1)+\alpha\left(k_y^2+2\varepsilon-2\right)\right)}{2\sqrt{2}(\alpha+1)} \\
-\frac{k_x k_y\left(\boldsymbol{k}^2+16\alpha-4\varepsilon+4\right)}{16(\alpha+1)} & G_{22} & \frac{i\left(2(\varepsilon-1)+\alpha\left(k_x^2+2\varepsilon-2\right)\right)k_y}{2\sqrt{2}(\alpha+1)} \\
\frac{ik_x\left(2(\varepsilon-1)+\alpha\left(k_y^2+2\varepsilon-2\right)\right)}{2\sqrt{2}(\alpha+1)} & -\frac{i\left(2(\varepsilon-1)+\alpha\left(k_x^2+2\varepsilon-2\right)\right)k_y}{2\sqrt{2}(\alpha+1)} & G_{33}
\end{pmatrix} \tag{6.62}$$

where

$$G_{11} = \left[1 - \frac{\boldsymbol{k}^2}{4} - 2\alpha + \varepsilon\right]\left[\frac{(2\alpha+1)k_y^2}{4(\alpha+1)} + \varepsilon - 1\right] - \frac{k_y^2}{2},$$

$$G_{22} = \left[\frac{(2\alpha+1)k_x^2}{4(\alpha+1)} + \varepsilon - 1\right]\left[1 - \frac{\boldsymbol{k}^2}{4} - 2\alpha + \varepsilon\right] - \frac{k_x^2}{2},$$

$$G_{33} = (\varepsilon-1)^2 + \frac{(2\alpha+1)\boldsymbol{k}^2(\varepsilon-1) + \alpha k_x^2 k_y^2}{4(\alpha+1)}.$$

and the determinant is given by the following third-order polynomial:

$$\det\left[\varepsilon - \frac{H^{(2)}_{SU(3)}(\boldsymbol{k})}{t_1}\right] = \varepsilon^3 - \frac{\varepsilon^2\left(\alpha\left(8\alpha - k^2 + 12\right) + \ 4\right)}{4(\alpha+1)}$$
$$- \frac{\varepsilon\left(-32(\alpha+1)(4\alpha-1) + \alpha k^4\cos(4\phi) + (3\alpha+2)k^4 + 16\alpha(2\alpha+1)k^2\right)}{32(\alpha+1)}$$
$$- \frac{128\left(2\alpha^2+\alpha-1\right) + \alpha k^6 + 4(\alpha-2)(2\alpha+1)k^4}{128(\alpha+1)}$$
$$+ \frac{32\alpha(4\alpha+1)k^2 + \alpha k^4\left(8\alpha + k^2 + 4\right)\cos(4\phi)}{128(\alpha+1)}. \tag{6.63}$$

These expressions were used above for the calculation of orbital susceptibility from the effective second-order model.